IOP Conference Series:
Materials Science and
Engineering

Importance of buoyancy flow in the macrosegregation formation during solidification of VAR process

To cite this article: Chenbo Xu *et al* 2025 *IOP Conf. Ser.: Mater. Sci. Eng.* **1335** 012021

Importance of buoyancy flow in the macrosegregation formation during solidification of VAR process

Chenbo Xu[1], Haijie Zhang[1,2], Christian Gomes-Rodrigues[1], Abdellah Kharicha[1], Menghuai Wu[1*]

[1]Chair of Modelling and Simulation of Metallurgical Processes, Department of Metallurgy, Montanuniversitaet Leoben, Franz-Josef Street 18, 8700 Leoben, Austria
[2]School of Mechanical and Materials Engineering, North China University of Technology, 100144, Beijing, China

*E-mail: menghuai.wu@unileoben.ac.at

Abstract. Vacuum arc remelting (VAR) is one of the most important processes to refine metal alloys and is also popularly used in the production of titanium alloys. However, due to the effect of electromagnetic forces, macrosegregation can occur in ingots. This study employs a volume average mixed columnar-equiaxed solidification model to investigate flow phenomena and their interaction with columnar solidification. The formation of equiaxed crystals due to fragmentation is here ignored, and to be considered in the future work. The flow is mainly driven by self-induced and external electromagnetic forces, but thermo-solutal buoyancy plays also the important role. A multicomponent titanium alloy is simplified as an equivalent binary alloy. The VAR ingot has a dimension of Φ 300 mm × 1000 mm. The results show that the electromagnetic forces operate dominantly in the upper part of the melt pool, while the thermo-solutal buoyancy operates in the lower part of the melt pool. Although the former induces much stronger flow than the latter, the role of the thermo-solutal buoyancy in the formation of macrosegregation is critical important. These insights contribute to a deeper understanding of the VAR process and can offer potential guidance for improving ingot quality.

1. Introduction

Vacuum arc remelting (VAR) is one of the most important processes for refining metal alloys and is widely employed in producing superalloys, high-performance steels, and titanium alloys. Among these, the titanium alloy is extensively used in key aerospace components, such as aircraft engine blades, owing to its exceptional strength, toughness, and fatigue resistance. As illustrated in Figure 1(a), the VAR process involves a consumable electrode (cathode) made from raw material and a water-cooled copper crucible serving as the anode. The consumable cathode is rapidly melted by a direct current arc, and the molten metal drips into the crucible, where it solidifies under vacuum to form an ingot. The defining characteristic of VAR is its controlled quasi-unidirectional upward solidification, which minimizes shrinkage porosity and macrosegregation. Experimental methods for mitigating freckles and macrosegregation, which heavily rely on empirical research experience, are not only costly but also prone to inconsistencies due to the influence of uncontrollable factors [1]. In contrast, numerical simulation provides a powerful alternative for investigating the formation mechanisms of these defects, because simulation results offer enhanced clarity and insight, enabling a more systematic and in-depth analysis [2]. Therefore, modeling studies were recently made and they provided valuable theoretical insights for understanding the macrosegregation mechanism [3,4].

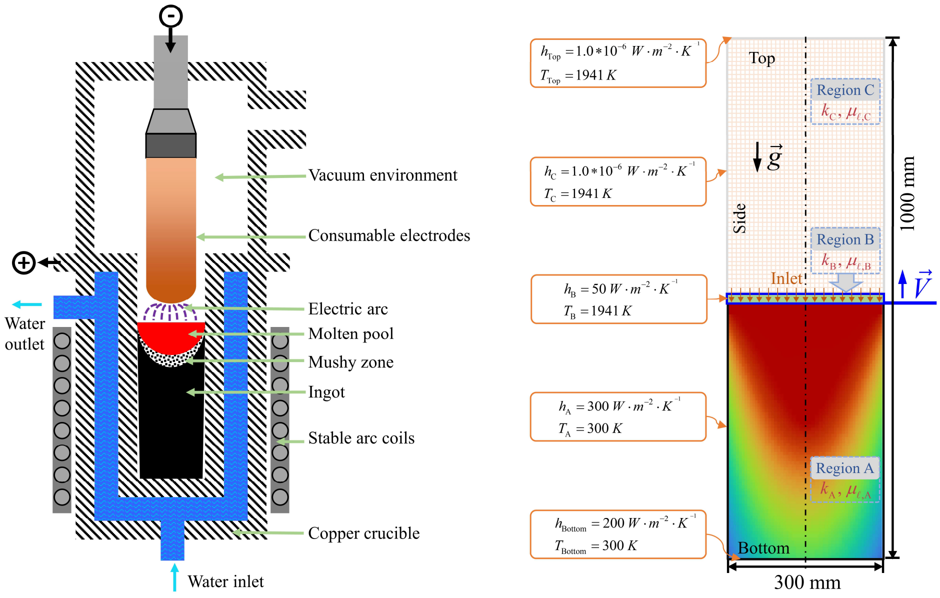

(a) (b)

Figure 1. Simulation configuration. (a) Schematic of VAR process, (b) Casting dimensions and boundary conditions.

In the present study, the solidification of a VAR ingot of titanium alloy is numerically simulated using a volume-average solidification model [5,6]. A 3D simulation is performed, accounting for the effects of thermo-solutal buoyancy force ($\vec{F}_B$), self-induced Lorenz force ($\vec{F}_L$), and stirring electromagnetic force ($\vec{F}_E$) generated by an externally applied alternating magnetic field (AMF). The primary objective is to investigate the influence of thermo-solutal buoyancy force on melt flow, and potential impact on the macrosegregation formation during the VAR process.

2. Modeling

The solidification process is simulated based on a volume average mixed columnar-equiaxed solidification model. Here only two phases, i.e., liquid and columnar, are considered. A multicomponent titanium alloy is simplified as an equivalent binary alloy (Ti – 15.1 wt.% C_{eq}), following the method suggested in the literature [7]. The Boussinesq approximation is used to account for the buoyancy force ($\vec{F}_B$). The way of coupling electromagnetic field with the solidification model follows the work of Kelkar [8]. The interaction between the electric current and its self-induced magnetic field generates a self-induced Lorentz force ($\vec{F}_L$). An alternative magnetic field (AMF) in the ingot axial direction is also applied, and it interacts with the remelting current $\vec{j}$ to generate an external stirring electromagnetic force ($\vec{F}_E$). The model was presented previously [5,6]. For brevity, it is not described here. Only parameters/properties are detailed in Table 1.

Table 1. Summary of material properties and other parameters [2,4,9].

Properties/parameters	**Symbol**	**Units**	**Values**
Thermophysical properties			
Specific heat	$c_{\mathrm{p}}^{\ell}, c_{\mathrm{p}}^{\mathrm{c}}$	$\mathrm{J \cdot Kg^{-1} \cdot K^{-1}}$	9.0×10^{2}
Latent heat	Δh_{f}	$\mathrm{J \cdot Kg^{-1}}$	2.85×10^{5}
Thermal conductivity	$k_{\mathrm{A}}, k_{\mathrm{B}}, k_{\mathrm{C}}$	$\mathrm{W \cdot m^{-1} \cdot K^{-1}}$	$34, 1.0\times10^{-2}, 1.0\times10^{-6}$
Viscosity	$\mu_{\ell,\mathrm{A}}, \mu_{\ell,\mathrm{B}}, \mu_{\ell,\mathrm{C}}$	$\mathrm{Kg \cdot m^{-1} \cdot s^{-1}}$	$3.05\times10^{-3}, 5.0\times10^{2}, 1.0\times10^{4}$
Liquid thermal expansion coefficient	β_{T}	$\mathrm{K^{-1}}$	-5.64×10^{-5}
Liquid solutal expansion coefficient	β_{c}	$\mathrm{wt.\%^{-1}}$	0.78×10^{-4}
Density	$\rho_{\ell}, \rho_{\mathrm{c}}$	$\mathrm{Kg \cdot m^{-3}}$	4025
Thermodynamic parameters			
Concentrations of binary eutectic valley	$c_{\mathrm{eut,C_{eq}}}^{*}$	-	0.98
Ternary eutectic temperature	T_{eut}	K	1850
Liquidus slope	$m_{\mathrm{C_{eq}}}$	$\mathrm{K\ (wt.\ \%)^{-1}}$	−0.925
Equilibrium partition coefficient	$k_{\mathrm{C_{eq}}}$	-	0.195
Melting point of solvent	T_{f}	K	1941
Other properties/parameters			
Initial concentrations	$c_{0,\mathrm{C_{eq}}}$	wt.%	15.1
Initial temperature	T_{0}	K	1941
Electrical conductivity	σ	$\mathrm{\Omega^{-1} \cdot m^{-1}}$	1.0×10^{6}
Magnetic permeability	μ	$\mathrm{H \cdot m^{-1}}$	3.65×10^{-6}
Remelting current	$I_{\mathrm{Remelting}}$	kA	3.0
Remelting velocity	$\vec{V}_{\mathrm{Remelting}}$	$\mathrm{m \cdot s^{-1}}$	3.85×10^{-4}
Arc stabilization current (AC)	I_{AC}	kA	1.0×10^{-3}
Period of AC	P_{AC}	s	20

*The superscript or subscript ℓ,c represent liquid phase and columnar phase, respectively, and the subscript A, B and C represent different regions of the calculation domain in Figure 1 (b).

The geometric configuration of the VAR simulation and thermal boundary conditions are illustrated in Figure 1(b). The transient remelting process of VAR ingot is numerically treated as follows. The 3-dimensional computational domain includes the entire geometry of the final ingot, Φ 300 mm ×1000 mm, which is discretised into 432697 volume elements with average cell size 5.46 mm. It is virtually divided into three regions A-C. All regions are initially filled with the melt of initial concentration and temperature. The solidification process occurs only in Region A with a moving 'inlet' located at the top surface of this region. Regions B and C are set as melt reservoir, providing fresh melt through the 'inlet' into Region A, mimicking the transient VAR remelting process. The position of the 'inlet' moves upwards with $\vec{V}$ ($\vec{V} = \vec{V}_{\mathrm{Remelting}}$), and the thermal boundary condition varies accordingly.

3. Results and discussions

3.1 *Simulation Case I – considering buoyancy*

Case I considers the effects of $\vec{F}_{\mathrm{B}}$, $\vec{F}_{\mathrm{L}}$ and $\vec{F}_{\mathrm{E}}$. A quasi-steady state is reached approximately 2000 s after the initiation of the VAR process. Figure 2(a) show the 3D-morphology of the simulated temperature at 2000 s, and the isotherms are characterized by a distinct "V"-shaped morphology, which is also reflected in the shape of the molten pool. The area where the solid phase volume fraction f_s ranges from 0.01 to 0.9 is defined as the mushy zone. The distribution of liquid solute concentration in the ingot is shown in Figure 2(b). The liquid concentration c_ℓ is close to the eutectic concentration in the solidified region, and decreases with the solid volume fraction in the mushy zone. In the liquid region, $c_{\ell,\mathrm{C_{eq}}}$ is almost identical to the initial concentration of the solute. The $\vec{F}_\mathrm{B}$ depends on the temperature and solute distribution within the molten pool.

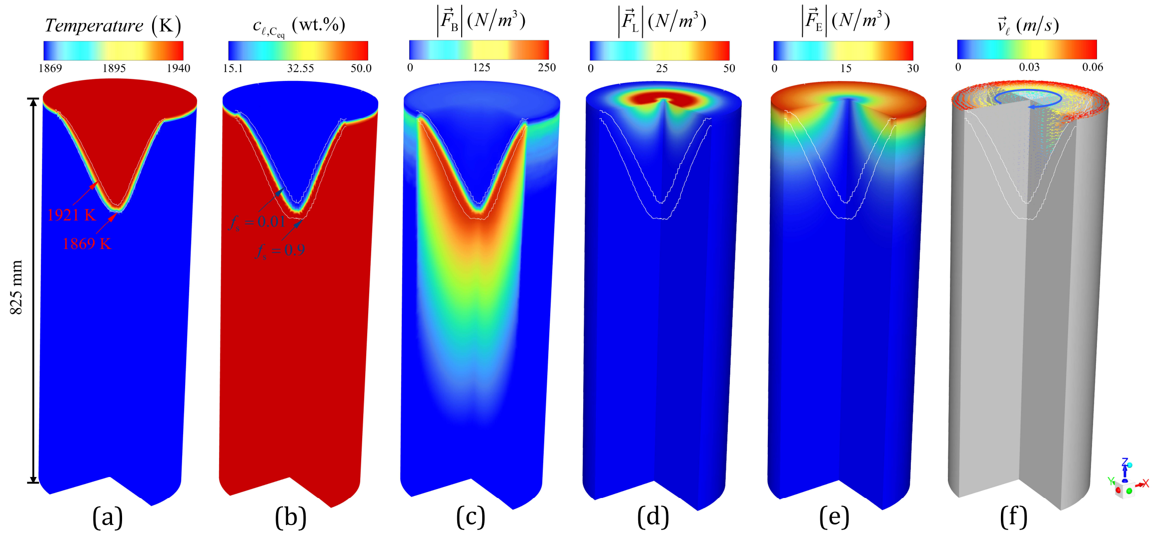

Figure 2. 3D-Simulation results under $\vec{F}_\mathrm{B}$, $\vec{F}_\mathrm{L}$ and $\vec{F}_\mathrm{E}$ with melting time of 2000 s. (a) temperature, (b) solute composition in Liquid phase, (c) modulus of $\vec{F}_\mathrm{B}$, (d) modulus of $\vec{F}_\mathrm{L}$, (e) modulus of $\vec{F}_\mathrm{E}$, (f) the distribution of $\vec{v}_\ell$.

According to Ampere's law, the interaction between the electric current $\vec{j}$ and the self-induced magnetic flux density $\vec{B}$ will produce a self-induced Lorentz force $\vec{F}_\mathrm{L}$ as shown in Figure 2(d). Additionally, the external stirring electromagnetic force $\vec{F}_\mathrm{E}$ generated by applying the external AMF is shown in Figure 2(e). Under the combined effect of $\vec{F}_\mathrm{B}$, $\vec{F}_\mathrm{L}$ and $\vec{F}_\mathrm{E}$, a rotating flow around the central axis appears in the molten pool, and the flow direction is shown by the blue arrow in the Figure 2(f).

A V-shaped molten pool is formed on the upper part of the casting. The mass transfer rate from the liquid to the columnar phase ($M_{\ell\mathrm{c}}$) is presented in Figures 3(a), and it can be seen that the phase transition occurs mainly near the columnar tip front. As solidification occurs, significant differences in temperature and liquid solute concentration fields appear in the mushy zone. The temperature and concentration gradients, along with the solute β_c and thermal β_T expansion coefficients, induce liquid flow due to $\vec{F}_\mathrm{B}$. In contrast to other forces, the flow velocity caused by $\vec{F}_\mathrm{B}$ is weaker. As depicted in Figure 3(b), $\vec{F}_\mathrm{L}$ is predominantly located in the upper portion of the molten pool, which acts toward the central axis of the ingot. Additionally, the applied external AMF interacts with the current density $\vec{j}$ to produce the external stirring force $\vec{F}_\mathrm{E}$, Figure 3(C). Different from $\vec{F}_\mathrm{L}$, $\vec{F}_\mathrm{E}$ acts in the tangential direction. Under the combined influence of $\vec{F}_\mathrm{B}$, $\vec{F}_\mathrm{L}$ and $\vec{F}_\mathrm{E}$, an obvious flow around the central axis appears in the upper part of the molten pool, Figure 3(d), reflecting that the liquid flow caused by $\vec{F}_\mathrm{E}$ at this moment dominates the liquid flow in the upper part of the molten pool. Compared with the Figure 3(c), the direction of liquid flow is not consistent with the direction of $\vec{F}_{\mathrm{E}}$. The reason is that the current in the external arc stabilization coils is alternating current, and the current period is 20 s, so the direction of the external stirring magnetic field also changes periodically. At this moment, $\vec{F}_{\mathrm{E}}$ just changes the direction. Due to the response lag of the liquid, the flow direction has not yet fully adjusted.

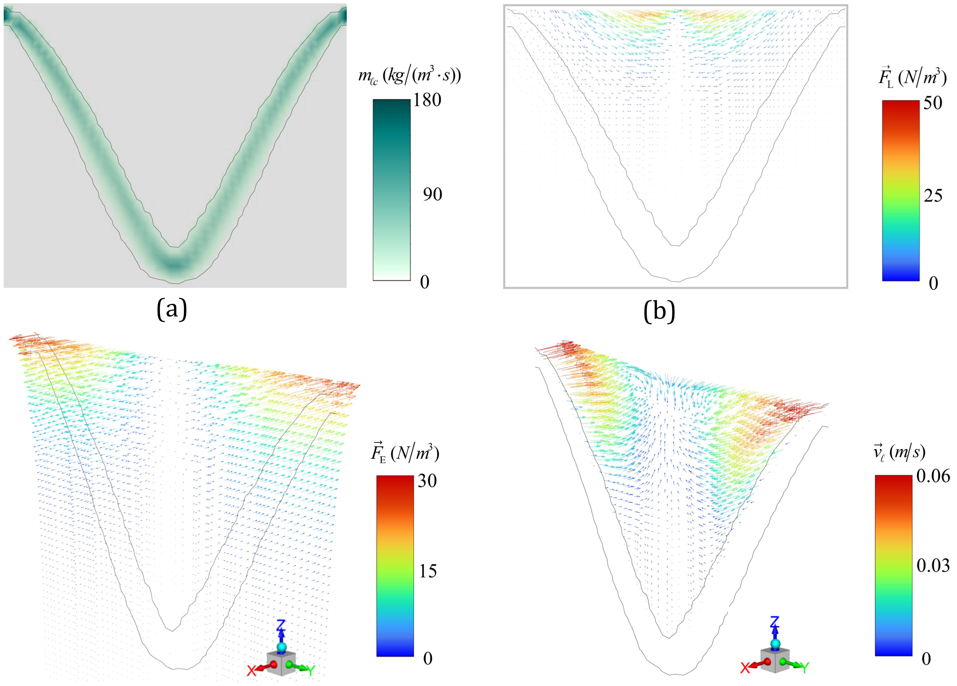

(a) (b)

(c) (d)

Figure 3. Various electromagnetic forces and liquid flow in the molten pool with melting time of 2000 s. (a) mass transfer rate, (b) the direction and distribution of $\vec{F}_{\mathrm{L}}$, (c) the direction and distribution of $\vec{F}_{\mathrm{E}}$, (d) the direction and distribution of $\vec{v}_\ell$.

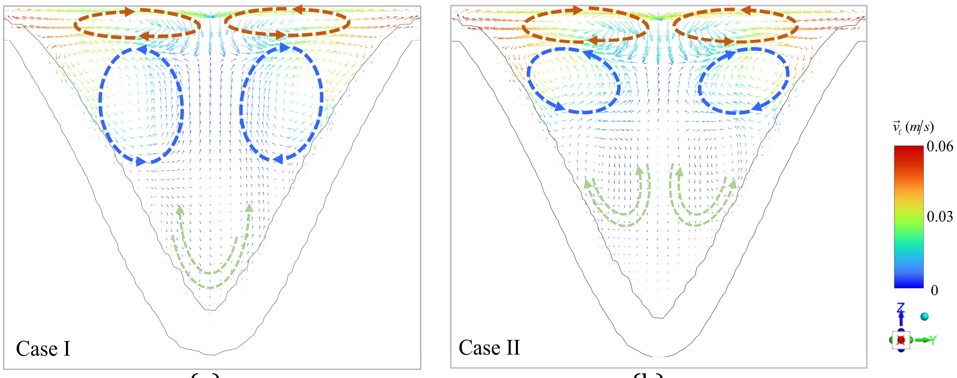

(a) (b)

Figure 4. Comparison between two cases of the liquid flow on the vertical section. (a) Case I under $\vec{F}_{\mathrm{B}}$, $\vec{F}_{\mathrm{L}}$ and $\vec{F}_{\mathrm{E}}$, (b) Case II under $\vec{F}_{\mathrm{L}}$ and $\vec{F}_{\mathrm{E}}$.

The liquid flow on the vertical section of the ingot is shown in Figure 4(a). Due to the effect of Ekman pumping [10], $\vec{F}_{\mathrm{E}}$ causes a vortex of "center-up, sidewall-down", as indicated by the blue arrow. The above flow morphology is qualitatively consistent with the results reported by Davison [11]. In addition, there is a vortex at the bottom of the molten pool, as shown by the green arrow. The liquid flow velocity induced by the electromagnetic forces is about 10 times stronger than that induced by thermo-solutal buoyancy. Compared with the results at other times, it can be found that the bottom of the molten pool has a periodic "reciprocating motion". This analysis highlights the intricate interplay of forces during the solidification of titanium alloy VAR ingots, underscoring the critical roles of electromagnetic force driven flow phenomena in influencing the resultant flow and thermal fields. In addition, the role of buoyancy cannot be ignored.

3.2 *Simulation Case II – without buoyancy*

This case ignores the effect of $\vec{F}_\mathrm{B}$ on liquid flow by setting both β_c and β_T to zero, but $\vec{F}_\mathrm{L}$ and $\vec{F}_\mathrm{E}$ are taken into account. Compared to the results of Case I, it can be found that ignoring $\vec{F}_\mathrm{B}$ has little effect on the solidification process and mushy zone of the ingot. However, it has a significant impact on the liquid flow in the molten pool. In case II, as shown in Figure 4(b), a pair of symmetrical vortices (green arrows) appears at the bottom of the molten pool. These vortices differ from the flow pattern displayed in Case I. Nonetheless, the direction of this vortices pair also changes periodically during the VAR process, which is not obtained in a 2D simulation.

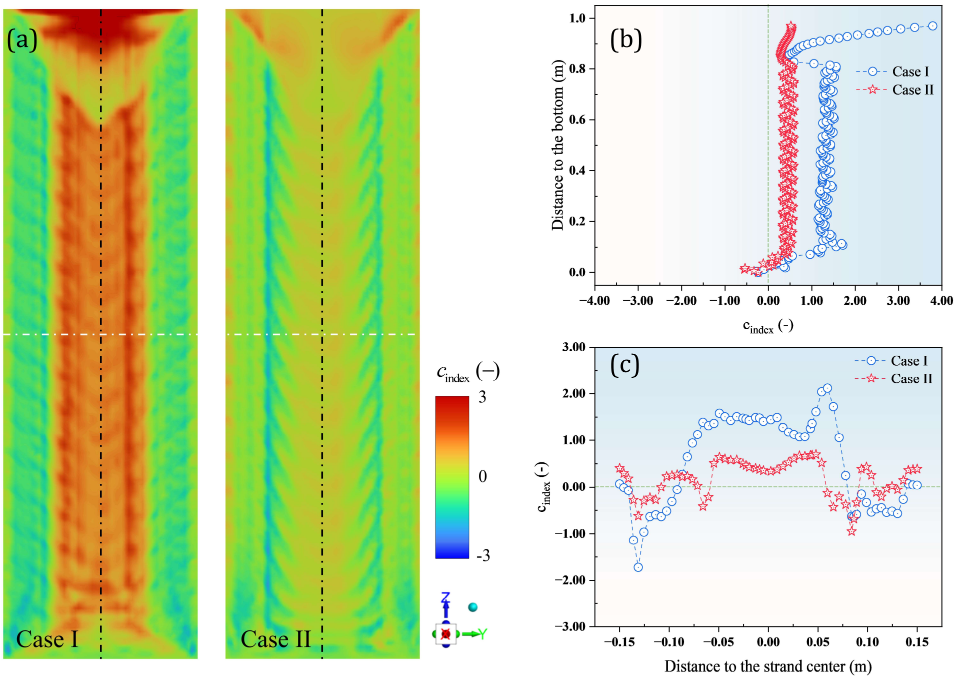

Figure 5. Macrosegregation of the final ingot. (a) The distribution of c_index, (b) the distribution c_index along the central axis, (c) the distribution c_index along the radial direction.

3.3 Macrosegregation

Macrosegregation is quantified by the segregation index c_index. It is calculated by $100\cdot\left(c_\mathrm{mix}-c_0\right)/c_0$, with $c_\mathrm{mix}=f_\ell c_{\ell,\mathrm{C_{eq}}}+f_\mathrm{s} c_{\mathrm{s},\mathrm{C_{eq}}}$. Figure 5(a) compares the macrosegregation distributions between the two cases. Solute enrichment occurs in the central region of the ingot, while a slight solute depletion occurs in the side region of the ingot in both cases. “Fishbone-shaped” segregation bands appeared in the central region of the ingot. The reason leading to this phenomenon is related to the periodical liquid flow in the molten pool. The electromagnetic forces $\vec{F}_\mathrm{L}$ and

$\vec{F}_{\mathrm{E}}$ operate dominantly in the upper part of the melt pool, while thermo-solutal buoyancy $\vec{F}_{\mathrm{B}}$ operates in the lower part of the melt pool. The reciprocating flow in the bottom region of the molten pool is not symmetrical when the effect of $\vec{F}_{\mathrm{B}}$ is considered (Case I). A single-direction liquid flow, which intensifies the liquid flow in front of the mushy zone, and the corresponding macrosegregation index in Case I is higher. Segregation profiles along the ingot centerline and across the radius direction are shown in Figure 5(b) and (c). Obviously, the segregation intensity of Case I is stronger than that of Case II, either along the centerline or across the radius section. This result highlights the importance of thermo-solutal buoyancy in the formation of macrosegregation. Although the flow induced by $\vec{F}_{\mathrm{L}}$ and $\vec{F}_{\mathrm{E}}$ is 10 times stronger than the $\vec{F}_{\mathrm{B}}$ induced flow, the former operates mainly in the upper part of the melt pool, while the latter operates in the lower region of the melt pool. The flow in the upper region has major effect on the global heat transfer in the melt pool, hence impacts very much on the shape of the melt pool. The flow in the lower region, which occurs at the late stage of the ingot solidification, impacts more effectively on the segregation intensity.

4. Conclusion and discussion

A volume average mixed columnar-equiaxed solidification model is implemented to simulate the solidification process of a VAR titanium ingot. The primary purpose of the study is to evaluate the model capability for calculating the complex melt flow and its impact to the macrosegregation formation. The transient remelting and solidification process must be considered, and different flow mechanisms due to self-induced and externally applied magnetic forces ($\vec{F}_{\mathrm{L}}$ and $\vec{F}_{\mathrm{E}}$) and thermo-solutal buoyancy ($\vec{F}_{\mathrm{B}}$) should be included. The nature of the flow pattern is 3-dimensional; hence a full 3D simulation is required. This preliminary modeling work shows a promising result. Although no systematic evaluation work was done yet, the predicted segregation profiles of Figure 5 show qualitative agreement with some industry experiments [2,12].

From the current modeling result, we find that the role of $\vec{F}_{\mathrm{B}}$ is critical important for the macrosegregation formation. Although the flow induced by $\vec{F}_{\mathrm{B}}$ is much weaker than that by $\vec{F}_{\mathrm{L}}$ and $\vec{F}_{\mathrm{E}}$, the $\vec{F}_{\mathrm{B}}$ induced flow operates in the lower part of the melt pool and close to the end position of the melt pool, hence it seems to impact more on the formation of macrosegregation.

The final goal of this study is to use the mixed columnar-equiaxed solidification model to simulate the industry VAR process for production of titanium alloy. As future work, following model features need to be included, such as the possible formation of equiaxed crystals by the mechanism of fragmentation [13] and freckles [14] in the VAR ingot, the mold-ingot contact and its influence on the electric current path [15], etc. Finally, the reliable thermal physical and process parameters are crucial for calculating the engineering process.

References

[1] Z. Yang, H. Kou, J. Li, et al. Macrosegregation behavior of Ti-10V-2Fe-3Al alloy during vacuum consumable arc remelting process, J. of Materi Eng and Perform 20 (2011) 65–70. https://doi.org/10.1007/s11665-010-9645-x.

[2] J. Han, N. Ren, Y. Zhou, et al. Melt convection and macrosegregation in the vacuum arc remelted Ti2AlNb ingot: Numerical methods and experimental verification, Journal of Materials Processing Technology 308 (2022) 117729. https://doi.org/10.1016/j.jmatprotec.2022.117729.

[3] P.F. Yun, J.H. Cao, Y.H. Shi, et al. Macrosegregation in vacuum arc remelted Ti-4.7Al-3V-2Mo-1.85Fe alloy: Industrial-scale ingot and numerical simulation, J. of Materi Eng and Perform (2025). https://doi.org/10.1007/s11665-025-10690-z.

[4] Z. Jing, R. Liu, N. Geng, et al. Simulation of solidification structure in the vacuum arc remelting process of titanium alloy TC4 based on 3d CAFE method, Processes 12 (2024) 802. https://doi.org/10.3390/pr12040802.

[5] M. Wu, A. Ludwig. Using a three-phase deterministic model for the columnar-to-equiaxed transition, Metall Mater Trans A 38 (2007) 1465–1475. https://doi.org/10.1007/s11661-007-9175-9.

[6] M. Wu, A. Ludwig, A. Kharicha. Volume-averaged modeling of multiphase flow phenomena during alloy solidification, Metals 9 (2019) 229. https://doi.org/10.3390/met9020229.

[7] H. Zhang, X. Liu, D. Ma, et al. Digital twin for directional solidification of a single-crystal turbine blade, Acta Materialia 244 (2023) 118579. https://doi.org/10.1016/j.actamat.2022.118579.

[8] K.M. Kelkar, S.V. Patankar, A. Mitchell, et al. Computational analysis of the vacuum arc remelting (VAR) and electroslag remelting (ESR) processes, in: D.U. Furrer, S.L. Semiatin (Eds.), Metals Process Simulation, ASM International, 2010: 196–213. https://doi.org/10.31399/asm.hb.v22b.a0005510.

[9] X. Wang, Z. Liu, F. Wang, et al. Effect of current intensity on molten pool and solidification in vacuum arc remelting process of Ti60 alloy, Ironmaking & Steelmaking: Processes, Products and Applications 51 (2024) 931–946. https://doi.org/10.1177/03019233241259280.

[10] P.A. Davidson, D. Kinnear, R.J. Lingwood, et al. The role of Ekman pumping and the dominance of swirl in confined flows driven by Lorentz forces, European Journal of Mechanics - B/Fluids 18 (1999) 693–711. https://doi.org/10.1016/s0997-7546(99)00106-5.

[11] P.A. Davidson, X. He, A.J. Lowe. Flow transitions in vacuum arc remelting, Materials Science and Technology 16 (2000) 699–711. https://doi.org/10.1179/026708300101508306.

[12] X. Liu, J. Shang, Y. Wu, et al. The morphology features, formation mechanism and elimination of channel segregation in industrial-scale Ti–Nb ingots produced by vacuum arc remelting, Journal of Materials Research and Technology 27 (2023) 5029–5040. https://doi.org/10.1016/j.jmrt.2023.11.009.

[13] Zheng, M. Wu., A. Kharicha, A. Ludwig. Incorporation of fragmentation into a volume average solidification model, Modell. Simul. Mater. Sci. Eng. 26 (2018) 015004. http://doi.org/10.1088/1361-651X/aa86c5.

[14] J. Shang, Y. He, C. Yang, et al. Freckles pattern and microstructure feature of Nb-Ti alloy produced by vacuum arc remelting, MATEC Web Conf. 321 (2020) 10009. https://doi.org/10.1051/matecconf/202032110009.

[15] E. Karimi-Sibaki, A. Kharicha, M. Abdi, et al. A numerical study on the influence of an axial magnetic field (AMF) on vacuum arc remelting (VAR) process, Metall Mater Trans B 52 (2021) 3354–3362. https://doi.org/10.1007/s11663-021-02264-w.